UNIVERSITY OF LEEDS

This is a repository copy of *How D-type H II region expansion depends on numerical resolution*.

White Rose Research Online URL for this paper:
https://eprints.whiterose.ac.uk/186667/

Version: Accepted Version

Article:

Pittard, JM orcid.org/0000-0003-2244-5070, Kupilas, MM orcid.org/0000-0002-6843-4521 and Wareing, CJ orcid.org/0000-0001-9641-0861 (2022) How D-type H II region expansion depends on numerical resolution. Monthly Notices of the Royal Astronomical Society, 510 (2). pp. 2797-2801. ISSN 0035-8711

https://doi.org/10.1093/mnras/stab3707

© 2021, Oxford University Press. This is an author produced version of an article published in Monthly Notices of the Royal Astronomical Society. Uploaded in accordance with the publisher's self-archiving policy.

Reuse

Items deposited in White Rose Research Online are protected by copyright, with all rights reserved unless indicated otherwise. They may be downloaded and/or printed for private study, or other acts as permitted by national copyright laws. The publisher or other rights holders may allow further reproduction and re-use of the full text version. This is indicated by the licence information on the White Rose Research Online record for the item.

Takedown

If you consider content in White Rose Research Online to be in breach of UK law, please notify us by emailing eprints@whiterose.ac.uk including the URL of the record and the reason for the withdrawal request.

White Rose
university consortium
Universities of Leeds, Sheffield & York

eprints@whiterose.ac.uk
https://eprints.whiterose.ac.uk/

How D-type H ii region expansion depends on numerical resolution

J. M. Pittard★, M. M. Kupilas and C. J. Wareing
School of Physics and Astronomy, University of Leeds, Woodhouse Lane, Leeds LS2 9JT, UK

Accepted 2021 December 16. Received 2021 December 16; in original form 2021 November 25

ABSTRACT

We investigate the resolution dependence of H ii regions expanding past their Strömgren spheres. We find that their structure and size, and the radial momentum that they attain at a given time, is in good agreement with analytical expectations if the Strömgren radius is resolved with $dr \leq 0.3\,R_{\rm st}$. If this is not satisfied, the radial momentum may be over- or under-estimated by factors up to 10 or more. Our work has significance for the amount of radial momentum that a H ii region can impart to the ambient medium in numerical simulations, and thus on the relative importance of ionizing feedback from massive stars.

Key words: hydrodynamics – methods: numerical – ISM: bubbles – H ii regions – ISM: kinematics and dynamics – galaxies: ISM

1 INTRODUCTION

Massive stars affect their surroundings through their ionizing radiation, powerful winds, and supernova (SN) deaths. These inputs heat and accelerate nearby gas, and can both compress and disperse gas clouds (e.g. Rogers & Pittard 2013; Kim et al. 2018; Wareing et al. 2018). As such, massive stars are recognized as key agents influencing star formation on both local and galactic scales. In recent years, attention has focused on the radial momentum that H ii regions, wind-blown bubbles, and supernova remnants can inject into the interstellar medium, since this determines the amplitude of gas motions which limit gravitational condensation and collapse (e.g. Shetty & Ostriker 2012).

Initial implementations of supernova feedback in galaxy and cosmology simulations used an energy injection approach, and suffered from an "over-cooling" problem caused by insufficient numerical resolution (e.g. Katz 1992). Only in the latest prescriptions has SN-driven feedback become independent of numerical resolution (e.g. the FIRE-2 algorithm implemented by Hopkins et al. 2018). Similarly, wind feedback has not always been adequately resolved. Pittard, Wareing & Kupilas (2021) showed that the wind injection radius must be below some maximum value, $r_{\rm inj,max}$, in order for the bubble momentum to closely agree with analytical predictions. Agreement within 25 per cent was obtained when $r_{\rm inj} = 0.1\,r_{\rm inj,max}$, and within 10 per cent when $r_{\rm inj} \lesssim 0.02\,r_{\rm inj,max}$.

We now turn our attention to ionizing feedback, which creates H ii regions around massive stars. Much numerical modelling of H ii regions exists in the literature, but we find that not all work has the necessary numerical resolution to capture the correct growth of the H ii region and its radial momentum. In this work we examine how the development of the H ii region depends on numerical resolution. We focus only on the ionizing feedback, so that other effects, such as the impact of the wind, for example, do not complicate the matter. In Sec. 2 we discuss the essential theory of H ii regions. In Sec. 3 we describe our calculations and our implentation of the photoionization microphysics. In Sec. 4 we present our results. We summarize and conclude in Sec. 5.

2 H ii REGION ESSENTIAL FEATURES

For simplicity we consider a star that emits ionizing photons at a constant rate $\dot{S}$ into a neutral medium of constant density and pressure. We assume that there are no dust grains or magnetic field. In reality, radiation pressure on dust and the dynamics of dust-gas coupling can be important for H ii region dynamics (Akimkin et al. 2017).

The ionizing photons ionize the neutral gas, and drive an ionization front that moves at a velocity $v_{\rm IF}$. Throughout this work we assume that any recombination to the ground state of hydrogen creates an ionizing photon with a very short mean free path and thus creates an ionization at roughly the same location (Osterbrock 1989). In this "on-the-spot" approximation the case B recombination coefficient is appropriate. If the neutral gas is molecular a dissociation front also moves outwards at a velocity $v_{\rm DF}$. At early times these fronts are coincident (Krumholz et al. 2007).

The ionization front expands very rapidly at first, and is known as R-type (Kahn 1954). Its radius increases as

$$r_{\rm IF} = R_{\rm st}\left(1 - e^{-t/t_{\rm rec}}\right)^{1/3}, \tag{1}$$

where $R_{\rm st}$ is the Strömgren radius given by (Strömgren 1939)

$$R_{\rm st} = \left(\frac{3\dot{S}}{4\pi\alpha_{\rm rr}^{\rm B} n_{\rm H}^2}\right)^{1/3}. \tag{2}$$

The recombination timescale, $t_{\rm rec} = 1/\alpha_{\rm rr}^{\rm B} n_{\rm H}$, is roughly the timescale for this first phase. The case B recombination coefficient is $\alpha_{\rm rr}^{\rm B} \approx 2.59 \times 10^{-13} (T/10^4\,{\rm K})^{-0.7}\,{\rm cm^3\,s^{-1}}$ (Osterbrock 1989; Rijkhorst et al. 2006), and $n_{\rm H}$ is the total hydrogen nucleon number density (molecular plus atomic plus ionized).

★ E-mail: j.m.pittard@leeds.ac.uk

© 2022 The Authors

The ionized gas has a substantially higher pressure than the surrounding neutral gas (mostly due to the increase in temperature, but also because of the increase in number density). This pressure increase causes the ionized gas to expand after a sound-crossing timescale. Around this time the ionization front changes from R-type to D-type. Because the ionization front moves at subsonic speed relative to the ionized gas but at supersonic speed relative to the neutral gas, it drives a shock front into the surrounding medium and sweeps up a dense shell of neutral material.

For $\dot{S} \gtrsim 10^{47}\,\mathrm{s}^{-1}$, the molecular hydrogen dissociation front does not have a significant effect on the dynamics, as it remains trapped between the ionization front and the shock front (Hosokawa & Inutsuka 2005; Krumholz et al. 2007). During the D-type expansion, Ritzerveld (2005) found that direct photons still dominate over diffuse ones and the on-the-spot approximation remains valid.

The shock radius in this second phase evolves as (Spitzer 1978; Hosokawa & Inutsuka 2006; Bisbas et al. 2015)

$$R_{\rm sh} = R_{\rm st}\left(1 + \frac{7}{4}\sqrt{\frac{4}{3}}\frac{c_{\rm i} t}{R_{\rm st}}\right)^{4/7}, \tag{3}$$

where $c_{\rm i}$ is the isothermal sound speed of the ionized gas. The shock velocity is given by

$$v_{\rm sh} = c_{\rm i}\sqrt{\frac{4}{3}\left(\frac{R_{\rm st}}{R_{\rm sh}}\right)^{3/2} - \frac{\mu_{\rm i} T_0}{2\mu_0 T_{\rm i}}}, \tag{4}$$

where T is the gas temperature, μ is the mean molecular weight, and subscripts “0” and “i” indicate the ambient and ionized medium respectively. The radial momentum of the shell swept-up by the expanding H II region is

$$p_{\rm sh} = \frac{4\pi}{3}(R_{\rm sh}^3 - R_{\rm st}^3)\rho_0 v_{\rm s}. \tag{5}$$

Eventually, the H II region attains pressure equilibrium with its surroundings. The radius at this time is (Raga, Cantó & Rodríguez 2012)

$$R_{\rm stag} = R_{\rm st}\left(\frac{8}{3}\right)^{2/3}\left(\frac{c_{\rm i}}{c_0}\right)^{4/3}, \tag{6}$$

where c_0 is the isothermal sound speed in the neutral medium.

3 THE CALCULATIONS

The Euler equations of gas dynamics for a spherically symmetric, inviscid and non-heat-conducting fluid may be written in Lagrangian coordinates in conservative form as follows (for the conservation of mass, momentum and energy, respectively):

$$\frac{\partial}{\partial t}\left(\frac{1}{\rho}\right) - \frac{\partial(r^2 u)}{\partial m} = 0, \tag{7}$$

$$\frac{\partial u}{\partial t} + r^2\frac{\partial p}{\partial m} = 0, \tag{8}$$

$$\rho\left[\frac{\partial E_{\rm m}}{\partial t} + \frac{\partial(r^2 u p)}{\partial m}\right] = \dot{E}_{\rm int,v}, \tag{9}$$

where ρ is the fluid mass density, u is the velocity and $E_{\rm m}$ is the total energy per unit mass. m is the mass coordinate defined as $dm = \rho r^2 dr$, where r is the radial coordinate. The internal energy per unit mass $e_{\rm m} = E_{\rm m} - u^2/2$, and the pressure $p = (\gamma - 1)\rho e_{\rm m}$. The source term on the right-hand side of the energy equation, $\dot{E}_{\rm int,v}$, is the internal energy change per unit volume, and represents cooling and heating processes that are discussed below.

We use a heavily modified version of VH-1[1] to solve Eqs. 7-9. The interface values are obtained via piecewise parabolic spatial reconstruction of the cell-averaged quantities, with flattening as appropriate. A 2-shock approximate Riemann solver is then used to obtain the interface fluxes, based on averages over the domain of influence of the characteristics. The cell-averaged quantities are then updated and a conservative remap is used to place them back onto the original stationary Eulerian grid. The method is third-order accurate in space for smooth parts of the flow, and first-order at shocks. A Courant number of 0.6 is used.

An advected scalar is used to track the hydrogen ionization fraction, y. Advected scalars are unchanged by the Lagrangian step but are modified during the remap step. The neutral fraction $x = 1 - y$. The total H number density $n_{\rm H} = \rho/\mu_{\rm H}$, where $\mu_{\rm H}$ is the mean mass per H nucleon. The number density of neutral hydrogen nucleons is $n_{\rm HI} = x n_{\rm H}$, and the number density of ionized hydrogen is $n_{\rm HII} = y n_{\rm H}$. To calculate the electron number density, $n_{\rm e}$, we assume that He is singly ionized whenever H is (Mackey et al. 2015), and that C is always singly ionized due to the interstellar UV field (Rijkhorst et al. 2006). We assume that all of the metals are Carbon. The electron number density is then given by $n_{\rm e} = y(n_{\rm H} + n_{\rm He}) + n_{\rm C}$, where $n_{\rm He}$ and $n_{\rm C}$ are the Helium and Carbon number densities, respectively. We assume mass fractions $X_{\rm H} = 0.7381$, $X_{\rm He} = 0.2485$, and $X_{\rm C} = 0.0134$ for the abundances (cf. Grevesse et al. 2010).

Changes to the ionization of the gas and heating/cooling processes are included via an operator split step. The rate of change of the ionization fraction and the internal energy per unit volume are:

$$\dot{y} = A_{\rm pi}(1 - y) + A_{\rm ci} n_{\rm H} y (1 - y) - \alpha_{\rm rr}^{\rm B} n_{\rm H} y^2, \tag{10}$$

$$\dot{E}_{\rm int,v} = (\rho/m_{\rm H})\Gamma + \mathcal{G}_{\rm ph} - (\rho/m_{\rm H})^2\Lambda(T) - n_{\rm e} n_{\rm HII}\Lambda_{\rm rec}. \tag{11}$$

In Eq. 10, the terms on the right hand side are due to photoionization, collisional ionization and recombination. In Eq. 11, the terms on the right hand side are due to background heating, heating due to the photoionization process, gas cooling and recombination cooling.

The ionizing radiation model uses a photon conservative scheme. The photoionization rate coefficient, $A_{\rm pi}$, depends on the rate of ionizing photons entering the cell minus the rate leaving. The photoionization rate within the cell is given by

$$\dot{N}_{\rm ion} = \dot{S} e^{-\tau}(1.0 - e^{-d\tau}), \tag{12}$$

where τ is the optical depth to ionizing photons from the star to the inner edge of the cell, and $d\tau$ is the optical depth to ionizing photons in the cell. The optical depth

$$\tau = \int (1 - y)\,\sigma\, n_{\rm H} dl, \tag{13}$$

where $\sigma = 6.3 \times 10^{-18}\,\mathrm{cm}^2$ is the photoionization cross-section for neutral H at the ionizing threshold and dl is the path length. We then have $A_{\rm pi} = \dot{N}_{\rm ion}/n_{\rm HI} V$, where V is the cell volume. The collisional ionization rate coefficient is given by $A_{\rm ci} = 5.84 \times 10^{-11}\sqrt{y}\exp(-13.6/kT)\,\mathrm{cm}^3\,\mathrm{s}^{-1}$ for gas at temperature T.

We assume that each absorption of an ionizing photon results in a photoelectron with an energy $e_\Gamma = 2.4\,\mathrm{eV}$ (Whalen & Norman 2006). These heat the gas, giving a heating rate per unit volume $\mathcal{G}_{\rm ph} = e_\Gamma \dot{N}_{\rm ion}/V$. For the recombination cooling we use $\Lambda_{\rm rec} = 6.1 \times 10^{-10} kT^{0.11}\,\mathrm{erg\,cm}^3\,\mathrm{s}^{-1}$ if $T \gtrsim 100\,\mathrm{K}$ (Osterbrock 1989). The cooling curve, $\Lambda(T)$, is constructed from 3 separate parts (see also Wareing et al. 2017a,b; Kupilas et al. 2021). At low temperatures

---

[1] http://wonka.physics.ncsu.edu/pub/VH-1/

($T < 10^4$ K) we use a fit to the data in Koyama & Inutsuka (2002), corrected by Vazquez-Semadeni et al. (2007):

$$\frac{\Lambda}{\Gamma} = 10^7 \exp\left(\frac{-1.184\times 10^5}{T+1000}\right) + 0.014\sqrt{T}\exp\left(\frac{-92}{T}\right). \tag{14}$$

For $10^4 \leq T/\mathrm{K} < 10^{7.6}$, $\Lambda(T)$ is constructed using data from CLOUDY v10.0 (Gnat & Ferland 2012). For $T \geq 10^{7.6}$ K, we use data from the MEKAL plasma emission code (Mewe, Kaastra & Liedahl 1995). We use a constant heating coefficient ($\Gamma = 2\times10^{-26}\,\mathrm{erg\,s^{-1}}$).

A temperature-dependent average particle mass, μ, is used. In the molecular phase $\mu = 2.36$, while $\mu = 0.61$ in ionized gas. The value of μ is determined from a look-up table of values of p/ρ (Sutherland 2010). The ratio of specific heats is set as $\gamma = 5/3$ at all temperatures.

In the operator split step we integrate x and $E_{\rm int,v}$ using the CVODE solver from the SUNDIALS v5.8.0 numerical library[2]. CVODE is a sophisticated solver that automatically detects stiffness. Like Mackey (2012), we find that the numerical integration is more stable if x rather than y is integrated. Because the ray-tracing is performed once per step, the photon conservation is first-order accurate in time, and our photoionization algorithm is the same as method A2 in Mackey (2012). We also set the same error tolerances for the CVODE solver (a relative error of 10^{-4} and absolute errors of 10^{-12} and 10^{-17} for x and $E_{\rm int,v}$, respectively). Following Mackey (2012), we also limit the timestep of the microphysics to

$$\Delta t = \min\left(K_1 t_{\rm rec}, K_2\frac{E_{\rm int,v}}{|\dot{E}_{\rm int,v}|}, K_3\frac{\max(0.05, 1-y)}{|\dot{y}|}, K_4\frac{1}{|\dot{y}|}\right). \tag{15}$$

In all of our calculations we set $K_1 = K_4 = \infty$ and $K_2 = K_3 = 0.3/\tau_{\rm cell}$, where $\tau_{\rm cell}$ is the initial optical depth of each grid cell. We use the smallest of the Courant-limited and microphysics-limited timesteps to advance both the hydrodynamics and the microphysics (i.e. we do not super-sample the microphysics).

Other ionization schemes are available that are more sophisticated than our scheme. These include the second-order explicit method A3 in Mackey (2012), and implicit schemes, such as C^2-ray (Mellema et al. 2006) and method A1 in Mackey (2012). However, because of the nature of the PPMLR hydrodynamics scheme used in this work, a first-order photoionization scheme is appropriate here. We do not expect our conclusions to be affected by our choice of scheme.

Naively, one might expect that the Strömgren radius should be resolved in order that the H II region expand correctly. Therefore, our focus is around this numerical resolution and we define

$$\chi = \frac{dr}{R_{\rm st}}, \tag{16}$$

where dr is the width of the grid cells. We then vary the value of χ in our simulations.

4 RESULTS

We adopt the following set of parameters for all of our simulations. We assume that $\dot{S} = 10^{49}\,\mathrm{s^{-1}}$ and $\rho_0 = 2\times10^{-21}\,\mathrm{g\,cm^{-3}}$ ($n_{\rm H} = \rho_0/\mu_{\rm H} = 884\,\mathrm{cm^{-3}}$, given a mean mass per H nucleon $\mu_{\rm H} = 2.26\times10^{-24}$ g). Our adopted value of ρ_0 determines that $\mu_0 = 2.36$ and $T_0 = 21$ K. The pressure of the ambient gas, $p_0 = 1.48\times10^{-12}\,\mathrm{dyn\,cm^{-2}}$ (or $p_0/k = 1.07\times10^4\,\mathrm{K\,cm^{-3}}$). This then gives $c_0 = 5.3\times10^4\,\mathrm{cm\,s^{-1}}$. We find that the temperature of the ionized gas $T_{\rm i} \approx 8100$ K, giving $c_{\rm i} \approx 1.04\times10^6\,\mathrm{cm\,s^{-1}}$. The mean molecular weight in the ambient and ionized gas is $\mu_0 = 2.36$ and $\mu_{\rm i} = 0.61$, respectively.

Table 1. The models investigated. The columns show the model name, the grid resolution, the ratio of the grid resolution to the Strömgren radius (Eq. 16), and the measured radial momentum of the H II region after 5 Myr.

Model	dr (pc)	χ	$p_{\rm sh}$ ($\mathrm{M_\odot\ km\,s^{-1}}$)
chi0.1	0.0702	0.1	2.78×10^5
chi0.3	0.211	0.3	2.86×10^5
chi1.0	0.702	1.0	3.12×10^5
chi3.0	2.11	3.0	3.57×10^5
chi5.0	3.51	5.0	4.03×10^5
chi7.5	5.27	7.5	3.33×10^5
chi10	7.02	10	6.88×10^4
chi30	21.1	30	2.01×10^4

The Strömgren radius, $R_{\rm st} = 0.702$ pc. Due to the large ratio of $c_{\rm i}/c_0$, the stagnation radius $R_{\rm stag} \approx 70$ pc. We evolve the simulations for 5 Myr, which is a typical lifetime for a massive star with an ionizing flux of this magnitude. Table 1 lists some other details of our models. In model *chi0.1*, each cell has a width $dr = 0.0702$ pc and an optical depth to ionizing photons $\tau_{\rm cell} = 1210$. The other models have larger cell widths and optical depths.

4.1 H II region profiles

Fig. 1 shows profiles of density, pressure, temperature and ionization fraction at $t = 5$ Myr for each of our models. In model *chi0.1*, we can clearly see the dense shell (at $r \approx 12$ pc) swept-up by the expanding H II region. Although the maximum density in the shell is not converged, with models with smaller values of χ showing higher values, the global properties are converged. The H II region is still a factor of 20 over-pressured with respect to the ambient medium at this time. Due to the compression of the gas in the swept-up shell, the temperature drops below 10 K. The ionization fraction of the gas drops away from unity only near the edge of the H II region. Waves within the H II region are also visible. These cause the density, velocity and pressure to oscillate, but the temperature and ionization fraction are largely unaffected. Waves are also seen in other work (e.g. see Fig. 4 in Bisbas et al. 2015). In our case they may also result from the PPMLR method employed by VH-1 where strong shocks that move slowly across the grid are known to cause strong oscillations.

As the resolution of the models change, the profiles begin to deviate from model *chi0.1*. The $\chi = 1$ model matches the higher resolution models reasonably well, and the $\chi = 3$ model still displays their main qualitative features despite not resolving the Strömgren radius. It is clear, therefore, that models with $\chi > 1$ may still create a H II region. In such cases, gas in the grid cell closest to the star becomes partially photoionized (from a greater to a lesser degree as χ increases). This raises the cell pressure which initiates a flow of gas out of the grid cell. The density in the grid cell drops, which allows the ionization fraction to increase further. In model *chi3.0*, this process runs-away on a timescale determined by the decreasing sound-crossing time of the gas as the cell changes from partially to fully ionized. The result is that model *chi3.0* creates a H II region with features qualitatively similar to higher resolution models by $t = 5$ Myr.

In contrast, models with $\chi \gtrsim 10$ fail to create completely ionized gas with $y = 1.0$ and $T = 8100$ K at $t = 5$ Myr in the grid cell closest to the star. The ionization fraction of this gas is 2.8% and 0.08% in

---

[2] https://computing.llnl.gov/projects/sundials

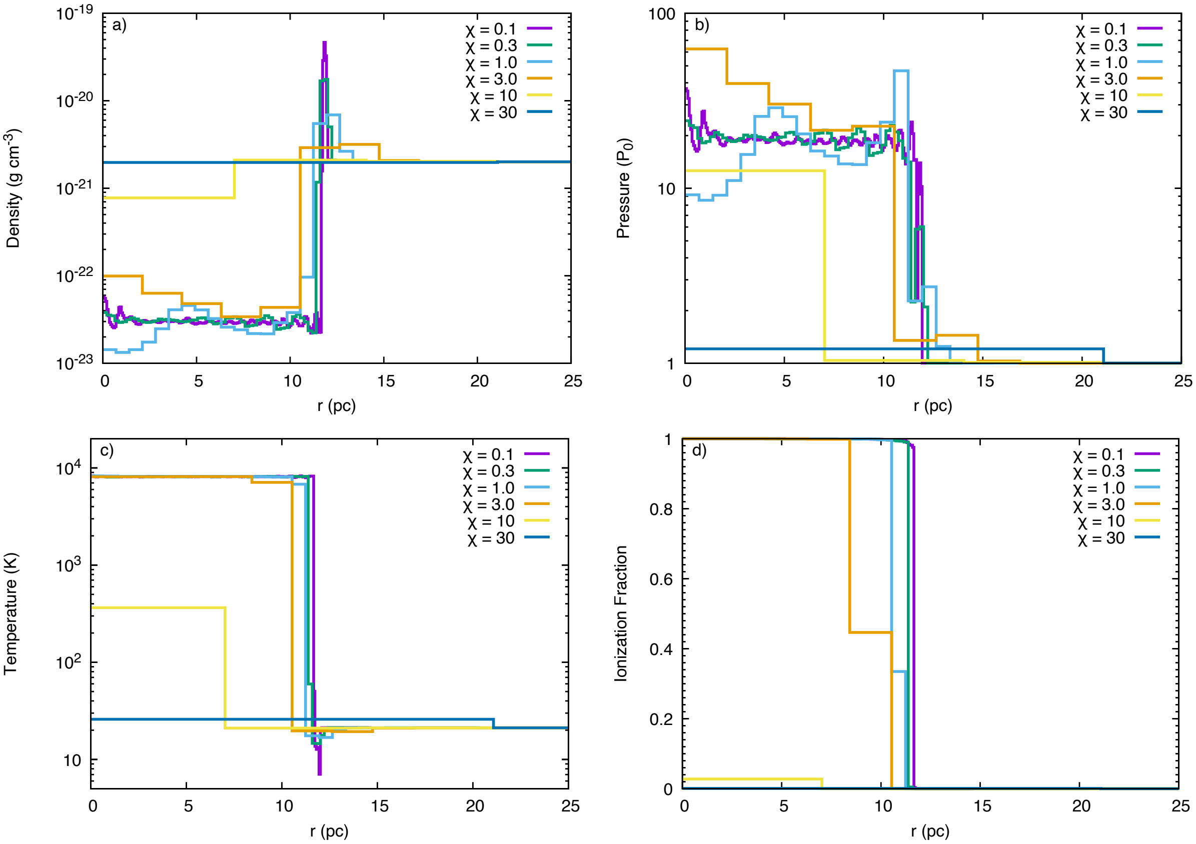

Figure 1. Profiles of a) density; b) pressure; c) temperature; and d) ionization fraction at $t = 5\,$Myr for models with $\chi = 0.1$, 0.3, 1.0, 3.0, 10 and 30. The ambient density and temperature values are visible on the far right of the plots in panels a) and c). Note the differences in the profiles as the resolution is varied. To aid the reader the plot style is deliberately chosen to show steps, as this displays the cell averaged quantity over the radii encompassed by each cell. In model *chi30* the cell width is 21.1 pc, so values from only two cells are visible.

models *chi10* and *chi30* respectively. Nevertheless, in both cases the partially ionized gas is able to initiate a flow away from the star due to the pressure difference that exists between it and the ambient gas. At $t = 5\,$Myr, the ratio of p/p_0 is 12.1 and 1.21 in models *chi10* and *chi30*, respectively.

4.2 Hɪɪ region size and momentum evolution

Fig. 2a) shows the shock front radius in models with $\chi \leq 1$. The shock front position is calculated as follows. We find the cell with the highest density and examine cells either side to see if they have any excess mass, δm (i.e if $\rho > \rho_0$). Those cells that have excess mass are included in the summations to obtain a mass weighted radius ($r = \sum \delta m r_{\rm cell}/\sum \delta m$, where $r_{\rm cell}$ is the radius of the centre of the grid cell). The shock radius from models with $\chi > 1$ is very dependent on the particular algorithm and so are not shown. For the models shown in Fig. 2a), the shock front radius compares well with analytical expectations.

Fig. 2b) shows the radial momentum of the Hɪɪ region, calculated by summing over *every* grid cell, including those past the shock front. Careful checks were made to ensure that small random velocity perturbations to the ambient gas due to numerical round-off error did not make any significant contribution to the measured momentum. Simulations with identical resolution but a different number of grid cells also confirm that this is the case.

It is immediately clear from Fig. 2b) that the simulations show some complex behaviour. Models with $\chi < 1$ are in good agreement with analytical expectations over the whole timescale considered. In models *chi1.0* and *chi3.0* the radial momentum is over-estimated at early times but converges towards the analytical solution at late times. In model *chi5.0* the radial momentum is over-estimated at mid-late times. Models with $\chi \geq 10$ show a dramatic reduction in the radial momentum at all times considered. Interestingly, we see that the model with $\chi = 7.5$ initially underestimates the radial momentum, but that there is a rapid increase between $t = 2 - 3\,$Myr. This timing is consistent with the initial sound crossing time of the gas in the grid cells of 9.7 Myr (an upper limit, with this timescale dropping as the gas heats). It appears that the *chi10* model is also heading for a similar rapid rise.

Table 1 lists the radial momentum from each model at $t = 5\,$Myr. The radial momentum obtained from Eq. 5 is $p_{\rm sh} = 3.32 \times 10^5\ {\rm M}_\odot\ {\rm km\,s^{-1}}$. As already noted, the momentum measured from model *chi0.1* is in good agreement with it.

5 SUMMARY AND CONCLUSIONS

We have examined the effect of numerical resolution on the D-type expansion of Hɪɪ regions. We find that a Hɪɪ region can be created, expand, and attain a radial momentum in good agreement with analytical predictions if the Strömgren radius is resolved such that $\chi = dr/R_{\rm st} \leq 0.3$. With $\chi = 1.0$ the radial momentum is overestimated at early times. Models with higher values of χ either over-

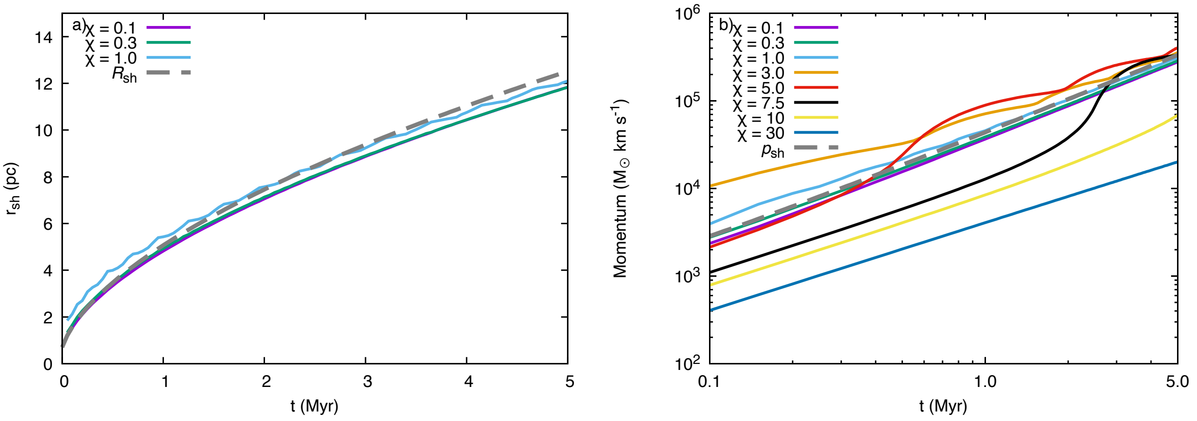

Figure 2. a) The radius of the shock front as a function of time for models with $\chi \leq 1$. b) The radial momentum of the HII region as a function of time for each model. The lines labelled $R_{\rm sh}$ and $p_{\rm sh}$ are calculated using Eqs. 3 and 5, respectively.

estimate, or significantly underestimate the radial momentum. For $\chi = 10$ and $\chi = 30$, the final radial momentum measured from our models is reduced by factors of 4 and 14, respectively.

Not all numerical simulations in the published literature seem to resolve the Strömgren radius. Amongst the SILCC group of papers, Peters et al. (2017) were the first to consider photoionization feedback. The SILCC models have a resolution of $dx = 3.9$ pc. In their model FRWSN (which also includes wind feedback), the sink particles are star clusters with a typical mass of 10^3 $M_\odot$. These clusters have an ionizing luminosity $L_{\rm ion} \sim 10^{39}$ erg s^{-1}, which corresponds to $\dot{S} \sim 5 \times 10^{49}$ s^{-1}. Since the sink particles are created above a density threshold $\rho = 2 \times 10^{-20}$ g cm^{-3}, we estimate that $R_{\rm st} \approx 0.2$ pc. This gives $\chi \approx 20$.

In another paper, Butler et al. (2017) describe kpc-scale zoom simulations of a galactic disk. The resolution is 0.5 pc. Sink particles are generated in cells where $n > 10^5$ cm^{-3}. They are born with a mass of 100 $M_\odot$ and IMF-averaged stellar evolution tracks are then followed. No accretion takes place onto the star particles. Rosdahl et al. (2015) shows that $L_{\rm UV}/M_\odot = 10^{36}$ erg s^{-1}, so each star particle has an ionizing flux $\dot{S} \sim 5 \times 10^{48}$ s^{-1}. The resulting Strömgren radius is $R_{\rm st} \sim 0.02$ pc. This gives $\chi \approx 25$.

In both of these papers, the resolution is likely to be too low for the HII reigons to grow correctly (unless they are clustered together). We stress that these papers are simply ones that we are familiar with; other work may suffer also from this problem. In scanning the literature we have sometimes found it hard to determine a value for the Strömgren radius given the information presented. We hope that future numerical work will explicitly demonstrate that the Strömgren radius is sufficiently resolved (i.e. $\chi \lesssim 0.3$).

A further complication is that in both reality and in numerical simulations, the HII region is typically interacting with a very inhomogeneous medium. In such cases the HII region will expand more quickly into regions of lower density, and vice-versa. While the global behaviour of the HII region can likely be represented by an averaged density for the local environment, it is not immediately clear how the radial momentum attained in such circumstances may differ from the spherically symmetric case. Further study of such a scenario is therefore warranted.

ACKNOWLEDGEMENTS

We thank the referee for their helpful comments. JMP was supported by grant ST/P00041X/1 (STFC, UK).

REFERENCES

Akimkin V. V., Kirsanova M. S., Pavlyuchenkov Ya. N., Wiebe D. S., 2017, MNRAS, 469, 630
Bisbas T. G., et al., 2015, MNRAS, 453, 1324
Butler M. J., Tan J. .C., Teyssier R., Rosdahl J., Van Loo S., Nickerson S., 2017, ApJ, 841, 82
Gnat O., Ferland G. J., 2012, ApJS, 199, 20
Grevesse N., Asplund M., Sauval A. J., Scott P., 2010, Ap&SS, 328, 179
Hopkins P. F., Wetzel A., Kereš D., Faucher-Giguère C.-A., Quataert E., Boylan-Kolchin M., Murray N., Hayward C. C., El-Badry K., 2018, MNRAS, 477, 1578
Hosokawa T., Inutsuka S., 2005, ApJ, 623, 917
Hosokawa T., Inutsuka S., 2006, ApJ, 646, 240
Kahn F. D., 1954, Bull. Astron. Inst. Neth., 12, 187
Katz N., 1992, ApJ, 391, 502
Kim J.-G., Kim W.-T., Ostriker E. C., 2018, ApJ, 859, 68
Koyama H., Inutsuka S., 2002, ApJ, 564, L97
Krumholz M. R., Stone J. M., Gardiner T. A., 2007, ApJ, 671, 518
Kupilas M. M.., Wareing C. J., Pittard J. M., Falle S. A. E. G., 2021, MNRAS, 501, 3137
Mackey J., 2012, A&A, 539, A147
Mackey J., Gvaramadze V. V., Mohamed S., Langer N., 2015, A&A, 573, A10
Mellema G., Iliev I. T., Alvarez M. A., Shapiro P. R., 2006, New Ast., 11, 374
Mewe R., Kaastra J. S., Liedahl D. A., 1995, Legacy, 6, 16
Osterbrock D. E., 1989, Astrophysics of Gaseous Nebulae and Active Galactic Nuclei (Mill Valley: University Science Books)
Peters T., Naab T., Walch S., Glover S. C. O., Girichidis P., Pellegrini E., Klessen R. S., Wünsch R., Gatto A., Baczynski C., 2017, MNRAS, 466, 3293
Pittard J. M., Wareing C. J., Kupilas M. M., 2021, MNRAS, 508, 1768
Raga A. C., Cantó J., Rodríguez L. F., 2012, Rev. Mex. Astron. Astrofis., 48, 149
Rijkhorst E.-J., Plewa T., Dubey A., Mellema G., 2006, A&A, 452, 907
Ritzerveld J., 2005, A&A, 439, L23
Rogers H., Pittard J. M., 2013, MNRAS, 431, 1337
Rosdahl J., Schaye J., Teyssier R., Agertz O., 2015, MNRAS, 451, 34
Shetty R., Ostriker E. C., 2012, ApJ, 754, 2
Spitzer L., 1978, Physical Processes in the Interstellar Medium, Wiley-Interscience, New York

Strömgren B., 1939, ApJ, 89, 526
Sutherland R. S., 2010, Ap&SS, 327, 173
Vazquez-Semadeni E., Gómez G. C., Jappsen A. K., Ballesteros-Paredes J., González R. F., Klessen R. S., 2007, ApJ, 657, 870
Wareing C. J., Pittard J. M., Falle S. A. E. G., 2017a, MNRAS, 465, 2757
Wareing C. J., Pittard J. M., Falle S. A. E. G., 2017b, MNRAS, 470, 2283
Wareing C. J., Pittard J. M., Wright N. J., Falle S. A. E. G., 2018, MNRAS, 475, 3598
Whalen D., Norman M. L., 2006, ApJS, 162, 281

This paper has been typeset from a TEX/LATEX file prepared by the author.